Available online at www.sciencedirect.com
SCIENCE DIRECT®
International Journal of Heat and Mass Transfer 47 (2004) 437–446
International Journal of HEAT and MASS TRANSFER
www.elsevier.com/locate/ijhmt

Large eddy simulation of heated vertical annular pipe flow in fully developed turbulent mixed convection

Joon Sang Lee, Xiaofeng Xu, Richard H. Pletcher *

Department of Mechanical Engineering, Iowa State University, 3024 Black Engr. Building, Ames, IA 50011, USA

Received 25 April 2003; received in revised form 25 July 2003

Abstract

The goal of the present study was to perform a large eddy simulation of vertical turbulent annular pipe flow under conditions in which fluid properties vary significantly, and to investigate the effects of buoyancy on the turbulent structures and transport. Isoflux wall boundary conditions with low and high heating are imposed. The compressible filtered Navier–Stokes equations are solved using a second order accurate finite volume method. Low Mach number preconditioning is used to enable the compressible code to work efficiently at low Mach numbers. A dynamic subgrid-scale stress model accounts for the subgrid-scale turbulence. Comparisons were made with available experimental data. The results showed that the strong heating and buoyant force caused distortions of the flow structure resulting in reduction of turbulent intensities, shear stress, and turbulent heat flux, particularly near the wall.
© 2003 Elsevier Ltd. All rights reserved.

Keywords: Large eddy simulation; Finite volume formulation; Compressible Navier–Stokes equations; Annular pipe flow

1. Introduction

Annular pipe flow is encountered in numerous engineering applications including gas-cooled nuclear reactors, heat exchangers, and advanced power reactors for both fission and fusion. These applications commonly employ turbulent flow with significant heat transfer resulting in large property variations. However, many proposed analytical and computational models provide poor predictions for convective heat transfer even when the properties can be idealized as constant [1], and it is very clear that the level of difficulty will be increased significantly if the property variations with buoyancy forces are considered. Flows in which the buoyancy force acts in the same direction as the flow are called aiding flows. When the directions are opposite, they are known as opposing flows. Nakajima and Fukui [2] studied a mixed convection flow experimentally and showed that the buoyancy force reduced the velocity fluctuations in the aiding flow case.

Polyakov [3] reported that the buoyancy forces modified the friction factor, the Nusselt number, and the velocity and temperature wall laws for turbulent heated flow in a vertical circular pipe. Zarate et al. [4] performed an experiment for the heated inner wall of a vertical concentric annular channel flow and found that the velocity and temperature data did not follow the respective wall laws when the influence of the buoyancy force became large.

Direct numerical simulation (DNS) and large eddy simulation (LES) provide means for obtaining detailed information about turbulent flows [5,6]. The present study deals with turbulent annular pipe flow with and without heat transfer. The influence of buoyancy on the mean and instantaneous structures is to be investigated. The present isothermal results are to be compared with streamwise mean velocity and root-mean-square (rms) DNS data [7]. Nusselt number correlations of experimental results [8,9] are also used for the code verification.

* Corresponding author. Tel.: +1-515-294-2656; fax: +1-515-294-3261.
E-mail address: pletcher@iastate.edu (R.H. Pletcher).

0017-9310/$ - see front matter © 2003 Elsevier Ltd. All rights reserved.
doi:10.1016/j.ijheatmasstransfer.2003.07.010

Nomenclature

C_d, C_I	dynamic subgrid-scale model coefficients
C_p	constant pressure specific heat, coefficient of pressure
C_v	constant volume specific heat
D_h	hydraulic diameter
G	filter function
Gr	Grashof number
g	gravitational constant
H	total enthalpy ($= h + u_i u_i/2$)
h	heat transfer coefficient, or specific enthalpy
$\vec{i}$, $\vec{j}$, $\vec{k}$	unit vectors for Cartesian coordinate system
L_{ref}	reference length
L_x	streamwise length of pipe
Ma	Mach number
m	pseudo time index
Nu	Nusselt number ($= 2h(r_2 - r_1)/k$)
n	physical time index
ni, nj, nk	control volume number in streamwise, radius and circumferential directions
$\vec{n}$	unit normal vector
n_x, n_y, n_z	components of unit normal vector
p_p	periodic component of the pressure
Pr	Prandtl number ($= \mu C_p/k$)
Pr_t	turbulent Prandtl number
p	thermodynamic pressure
Q_j	subgrid-scale turbulent heat flux vector
Q_{tj}	test filtered heat flux vector
q_j	heat flux vector
q_{tj}	Favre filtered heat flux vector
q_w	nondimensional wall heat flux
R	gas constant
r	radius of pipe
Re	generic Reynolds number
S	magnitude of cell face area vector or skewness factor
$\vec{S}$	cell face area vector
S_{ij}	strain rate tensor
T	thermodynamic temperature
T_b	bulk temperature
T_{ij}	test filtered stress tensor
t	physical time
$[U]$	vector of conserved variables
u_τ	friction velocity ($= \sqrt{\tau_w/\rho_w}$)
u, v, w	Cartesian velocity components in x, r, θ directions
V_r	reference velocity
x, y, z	Cartesian coordinates

Greek symbols

β	volumetric thermal expansion coefficient
γ	ratio of specific heats
Δ	grid filter width
$\widehat{\Delta}$	test filter width
δ	Kronecker delta
ϵ	temperature difference ($= (T_{in} - T_b)/T_b$)
μ	molecular dynamic viscosity
μ_t	subgrid-scale turbulent viscosity
ν	molecular kinematic viscosity ($= \mu/\rho$)
ν_t	subgrid-scale turbulent kinematic viscosity
ρ	thermodynamic density
σ_{ij}	shear stress tensor
τ_{ij}	subgrid-scale stress tensor
Ω	cell volume

Subscripts

b	bulk property
i, j, k	indices for Cartesian coordinates
in	property near inner wall
out	property near outer wall
nw	near wall cell quantity
p	periodic component
r	associated with radius direction of pipe
rms	root-mean-square
w	wall value
x, y, z	associated with Cartesian direction
x, r, θ	associated with cylindrical direction

Superscripts and other symbols

$'$	fluctuation with respect to ensemble average, or unresolved or subgrid-scale component of filtered quantity
$-$	resolved or large scale component of filtered quantity
$\sim$	resolved or large scale component of Favre filtered quantity
$\wedge$	nonlinear function of Favre filtered quantity
$\langle\ \rangle$	ensemble averaged quantity

The Prandtl number was assumed to be 0.71 in this study. All cases employed a $4.5r \times 2r \times 2\pi r$ computational domain in the streamwise, radial, and circumferential directions, respectively, where r is the half-distance between the outer and inner wall radii. The buoyant force is shown to effect substantially the mean velocity, temperature, Nusselt number as well as turbulent intensities.

2. Governing equations

The numerical scheme employed in the present study solved the conservation equations formulated in the Cartesian coordinate system. Advantages of this approach include the following. First, the Cartesian based equations are as simple as possible and can be put in

strong conservation (or divergence) form. This generally helps toward maintaining accuracy since using the alternative coordinate-oriented systems such as the cylindrical or polar systems requires that the basis vectors change directions. This introduces an "apparent force" to cause the turning that is nonconservative in form and hard to represent accurately. Second, the equations in the cylindrical and polar systems contain singularities at the coordinate origin. It is true that grid-related singularities may also occur when the Cartesian-based equations are used, but these are usually easier to accommodate than singularities in the equations themselves.

For gas flows with property variations (density, viscosity, and thermal conductivity), the compressible Navier–Stokes (N–S) equations are applicable even if a low speed case is dealt with.

2.1. Compressible nondimensional Navier–Stokes equations

- Conservation of mass

$$\frac{\partial \rho}{\partial t} + \frac{\partial(\rho u_i)}{\partial x_i} = 0 \tag{1}$$

- Conservation of momentum

$$\frac{\partial(\rho u_i)}{\partial t} + \frac{\partial(\rho u_i u_j)}{\partial x_j} = -\frac{\partial p}{\partial x_i} + \frac{\partial \sigma_{ij}}{\partial x_j} - \frac{Ra}{(2\epsilon PrRe^2)}\delta_{1i} \tag{2}$$

- Conservation of energy

$$\frac{\partial(\rho E)}{\partial t} + \frac{\partial(\rho E u_j)}{\partial x_j} = -\frac{\partial(p u_j)}{\partial x_j} - \frac{\partial q_j}{\partial x_j} + \frac{\partial(\sigma_{ij} u_i)}{\partial x_j} - \frac{Ra}{(2\epsilon PrRe^2)}\rho u_i \delta_{1i} \tag{3}$$

where δ_{1i} is the Kronecker delta and the specific total energy is $E = e + 1/2 u_j u_j$.

The nondimensional heat flux vector is,

$$q_j = -\frac{C_p \mu}{PrRe}\frac{\partial T}{\partial x_j} \tag{4}$$

the dimensionless viscous stress term, σ_{ij}, is,

$$\sigma_{ij} = \mu\left(\frac{\partial u_i}{\partial x_j} + \frac{\partial u_j}{\partial x_i}\right) + \lambda\frac{\partial u_k}{\partial x_k}\delta_{ij} \tag{5}$$

ϵ is the temperature difference defined by

$$\epsilon = (T_{\text{in}} - T_{\text{b}})/T_{\text{b}} \tag{6}$$

where T_{in} and T_{b} represent the inner wall and bulk temperatures, respectively.

And the Rayleigh number, Ra, is,

$$Ra = \frac{2\epsilon g \rho_0^2 L_0^3 Pr}{\mu_0^2} \tag{7}$$

A perfect gas equation of state was used since the intermolecular forces were assumed to be negligible,

$$p = \rho RT \tag{8}$$

where R is the nondimensional gas constant. For the property evaluations, the following functions were used.

$$\mu = k = T^a \tag{9}$$

The exponent a has been taken as 0.71.

2.2. Filtering

To separate the large-scale (or resolved) variables, denoted by an over bar, from the small-scale variables, a filtering operation needs to be defined as

$$\bar{f}(x) = \int_D f(x')G(x,x')\,\mathrm{d}x' \tag{10}$$

where G is the filter function, and D is the entire domain.

There are three different forms of the filter function that have been used in CFD applications, the spectral cut-off, Gaussian, and top-hat functions. In this research, the top-hat function was used, and it is defined as

$$G(x) = \begin{bmatrix} 1/\Delta & \text{if } |x| \leqslant \Delta/2 \\ 0 & \text{otherwise} \end{bmatrix} \tag{11}$$

where Δ is the filter width given by $\Delta = (\Delta_x \Delta_y \Delta_z)^{1/3}$. Δ_x, Δ_y, and Δ_z are the control volume dimensions in the x, y, and z directions.

2.3. Mass-weighted (Favre) averaging

The unsteady compressible N–S equations are a mixed set of hyperbolic–parabolic equations in time, and it is possible to solve them for both low and high speed flow. However, the treatment of compressibility is not convenient unless mass-weighted averaging is used. To simplify the filtered equations, a Favre-averaging [10] is applied. This mass-weighted approach introduces the following new variables.

$$\tilde{f} = \frac{\overline{\rho f}}{\bar{\rho}} \tag{12}$$

where f is a general flow variable.

Generally, the variable can be decomposed as

$$f = \tilde{f} + \tilde{f}' \tag{13}$$

where $\tilde{f}$ and $\tilde{f}'$ are the Favre-averaged variables and its fluctuation, respectively.

The compressible N–S equations, Eqs. (1)–(3), are filtered and become

$$\frac{\partial \bar{\rho}}{\partial t} + \frac{\partial(\bar{\rho}\tilde{u}_j)}{\partial x_j} = 0 \tag{14}$$

$$\frac{\partial(\bar{\rho}\tilde{u}_i)}{\partial t}+\frac{\partial(\bar{\rho}\tilde{u}_i\tilde{u}_j)}{\partial x_j}=-\frac{\partial\bar{p}}{\partial x_i}+\frac{\partial\bar{\sigma}_{ij}}{\partial x_j}-\frac{Ra}{(2\epsilon PrRe^2)}\delta_{1i}-\frac{\partial\tau_{ij}}{\partial x_j} \tag{15}$$

$$\frac{\partial(\bar{\rho}\widehat{E})}{\partial t}+\frac{\partial[(\bar{\rho}\widehat{E}+\bar{p})\tilde{u}_j]}{\partial x_j} =-\frac{\partial(\tilde{u}_i\bar{\sigma}_{ij})}{\partial x_j}-\frac{\partial\bar{q}_j}{\partial x_j}-\frac{Ra}{(2\epsilon PrRe^2)}\bar{\rho}\tilde{u}_i\delta_{1i}-\frac{\partial q_{tj}}{\partial x_j}-\alpha-\pi-\varepsilon \tag{16}$$

where

$$\alpha=\tilde{u}_i\frac{\partial\tau_{ij}}{\partial x_j} \tag{17}$$

$$\pi=\overline{p\frac{\partial u_j}{\partial x_j}}-\bar{p}\frac{\partial\tilde{u}_j}{\partial x_j} \tag{18}$$

$$\varepsilon=\overline{\sigma_{ij}\frac{\partial u_i}{\partial x_j}}-\bar{\sigma}_{ij}\frac{\partial\tilde{u}_j}{\partial x_j} \tag{19}$$

For the present work, α, π and ε were neglected since only low Mach number flows were considered, which is an appropriate assumption for Mach numbers below 0.2 [11]. The filtered viscous stress tensor and heat flux vector are

$$\bar{\sigma}_{ij}=\frac{\bar{\mu}}{Re}\left[\left(\frac{\partial\tilde{u}_i}{\partial x_j}+\frac{\partial\tilde{u}_j}{\partial x_i}\right)-\frac{2}{3}\frac{\partial\tilde{u}_k}{\partial x_k}\delta_{ij}\right] \tag{20}$$

$$\bar{q}_j=-\frac{C_p\bar{\mu}}{RePr}\frac{\partial\widetilde{T}}{\partial x_j} \tag{21}$$

the turbulent stress tensor and heat flux vector are

$$\tau_{ij}=\bar{\rho}(\widehat{\tilde{u}_i\tilde{u}_j}-\tilde{u}_i\tilde{u}_j) \tag{22}$$

$$q_{tj}=\bar{\rho}C_v(\widehat{\tilde{u}_j\widetilde{T}}-\tilde{u}_j\widetilde{T}) \tag{23}$$

3. LES methodology and boundary conditions

3.1. Dynamic model

Dynamic modeling of the subgrid-scale stresses was introduced by Germano et al. [12]. Unlike the Smagorinsky model, the model coefficients, C_d, and C_I, are computed dynamically as the computation progresses. Before the dynamic model coefficients are introduced, a test filter should be given by

$$\hat{f}(x)=\int_D f(x')\widehat{G}(x,x')\,dx' \tag{24}$$

where $\widehat{G}$ is the test filter. In this work, the test filter was two times larger than the filter function G. The dynamic model for this research was based on Wang's [14] derivation. By use of Lilly's [15] approach, the unknown parameters, C_d, and C_I can be determined as

$$C_d=\frac{-1}{2\Delta^2}\frac{\langle D_{ij}P_{ij}\rangle}{\langle P_{ij}P_{ij}\rangle} \tag{25}$$

$$C_I=\frac{1}{\Delta^2}\frac{\langle\widehat{\bar{\rho}\tilde{u}_k\tilde{u}_k}-(\widehat{\bar{\rho}\tilde{u}_k}\widehat{\bar{\rho}\tilde{u}_k}/\hat{\bar{\rho}})\rangle}{\langle 2(\hat{\bar{\rho}}\alpha|\widehat{\bar{S}}|^2-\bar{\rho}|\widetilde{S}|^2)\rangle} \tag{26}$$

where $\langle\ \rangle$ denotes spatial averaging along the streamwise and spanwise directions of the flow, $|S|$ is the magnitude of strain rate tensor, Δ is the filtered width $(=(\Delta_x\Delta_y\Delta_z))^{1/3}$, and α is the strain grid ratio $(=\widehat{\bar{\Delta}}/\bar{\Delta})$. The superscripts $(\hat{},\bar{},\tilde{})$ denote the nonlinear function of a Favre filtered quantity, large scale component of filtered quantity, and large scale component of Favre filtered quantity, respectively. D_{ij} and P_{ij} are defined as

$$D_{ij}=\frac{\widehat{\bar{\rho}\tilde{u}_i\tilde{u}_j}-\widehat{\bar{\rho}\tilde{u}_i}\widehat{\bar{\rho}\tilde{u}_j}}{\hat{\bar{\rho}}}-\frac{1}{3}(T_{kk}-\widehat{\tau_{kk}})\delta_{ij} \tag{27}$$

$$P_{ij}=\hat{\bar{\rho}}|\widehat{\bar{S}}|\left(\widehat{\bar{S}}_{ij}-\frac{1}{3}\widehat{\bar{S}}_{kk}\delta_{ij}\right)-\left[\bar{\rho}|\widetilde{S}|\left(\widetilde{S}_{ij}-\frac{1}{3}\widetilde{S}_{kk}\delta_{ij}\right)\right] \tag{28}$$

Many researchers neglect the isotropic part of the SGS stress tensor on the grounds that it is not only negligible compared to the thermodynamic pressure, but also the calculation is unstable if the isotropic part of the SGS stress tensor is not neglected [11,13] Therefore, C_I is set to zero in this study.

The turbulent heat flux in the energy equation needs to be modeled following Wang [14].

$$q_{tj}=-\bar{\rho}\nu_H\frac{\partial\widetilde{T}}{\partial x_j} \tag{29}$$

where the SGS eddy heat diffusivity is

$$\nu_H=-\frac{C_d\bar{\Delta}^2}{Pr_t}|\widetilde{S}_{ij}| \tag{30}$$

and the turbulent Prandtl number (Pr_t) is

$$Pr_t=-C_d\bar{\Delta}^2\frac{\langle F_kF_k\rangle}{\langle E_kF_k\rangle} \tag{31}$$

E_k and F_k are defined as

$$E_k=\frac{1}{\hat{\bar{\rho}}}\widehat{\bar{\rho}\tilde{u}_k}\widehat{\bar{\rho}\widetilde{T}}-\widehat{\hat{\rho}\tilde{u}_k\widetilde{T}} \tag{32}$$

$$F_k=\widehat{\bar{\Delta}}^2\hat{\bar{\rho}}|\widehat{\bar{S}}|\frac{\partial\widehat{\widetilde{T}}}{\partial x_k}-\bar{\Delta}^2\bar{\rho}\widehat{|\widetilde{S}|\frac{\partial\widetilde{T}}{\partial x_k}} \tag{33}$$

3.2. Boundary conditions

The governing equations require specification of boundary conditions at the wall, inlet, and exit due to the elliptic nature of the equations. Nonslip wall conditions were imposed at the wall. Since fully developed

annular pipe flow was considered in this study, periodic and stepwise periodic boundary conditions were used at the inlet and outlet as follows,

$$\begin{aligned} p_p &= p_p(L_x, r) \\ \rho u(0, r) &= \rho u(L_x, r) \\ v(0, r) &= v(L_x, r) \\ w(0, r) &= w(L_x, r) \\ T(0, r) &= T(L_x, r) - \Delta T_x \end{aligned} \tag{34}$$

where p_p is the periodic component of the pressure, and L_x is the length of the channel in the streamwise direction. The nondimensional temperature difference, ΔT_x, was calculated by

$$\Delta T_x = \frac{(2\pi r_{\text{in}}) q_{\text{w}_{\text{in}}} L_x}{\dot{m}} \tag{35}$$

r_{in} is the nondimensional inner wall radius, L_x is the nondimensional length of the pipe in the streamwise direction, $\dot{m}$ is the nondimensional mass flow rate, and $q_{\text{w}_{\text{in}}}$ is the dimensionless inner wall heat flux.

The inner wall of the annular pipe was heated with constant heat flux. The isoflux thermal boundary condition is typically implemented by setting

$$T_{\text{in}} = T_{\text{nw}_{\text{in}}} + \frac{\Delta y q_{\text{w}_{\text{in}}}}{k} \tag{36}$$

where the subscript, nw, denotes the near wall value. But using Eq. (36) can generate the unrealistic nonzero fluctuations near the solid wall. The alternative method, specifying a linear distribution of temperature, was used. The parameters for the linear distribution can be determined by running several trials using Eq. (36).

The adiabatic boundary condition ($q_{\text{w}_{\text{out}}} = 0$) was applied for the outer wall throughout this study.

4. Finite volume approach

A coupled finite volume method was used to solve the filtered compressible NS equations based on Cartesian coordinates. This approach has been successfully tested on planar channel flow with Cartesian hexahedral control volumes [16]. The finite volume formulation used here is valid for general, non-Cartesian control volumes.

The control volume is defined as shown in Fig. 1 and the primitive variables p, u_i and T are stored at the cell centers. The surface integral was approximated as,

$$\oint_S \vec{F} \cdot \mathrm{d}\vec{S} = \sum_{\beta=1}^{k} [(F_x n_x + F_y n_y + F_z n_z) S]_\beta \tag{37}$$

where $\vec{F}$ is the flux vector at a point on the surface, $\mathrm{d}\vec{S}$ is the surface normal at that point, β denotes the k surfaces of the control volumes and (n_x, n_y, n_z) are the Cartesian components of the unit outward normal to the surface.

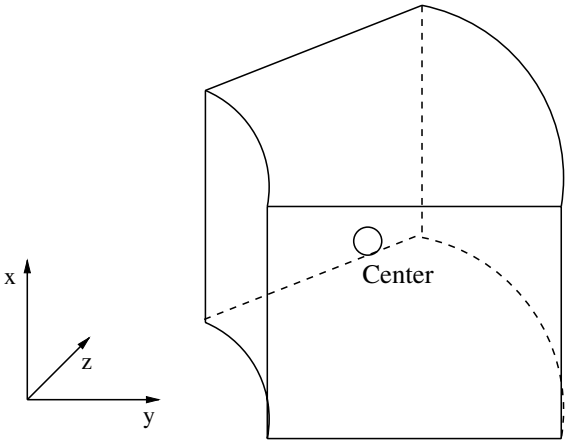

Fig. 1. Sketch of control volumes.

Gradients were calculated using the Gauss divergence theorem,

$$\int_{\Omega'} \nabla \phi \, \mathrm{d}\Omega' = \oint_{\partial\Omega'} \phi \, \mathrm{d}\vec{S}' \tag{38}$$

where ϕ is a scalar, Ω' is the volume of auxiliary control volume which was obtained by shifting the main control volume a half index in the direction of the surface on which the gradients were calculated.

Time-derivative preconditioning was used to enable the computation of low Mach number flows with property variations. Time integration was performed using the implicit LU-SGS scheme [17] with a dual time stepping approach and the solver was second order accurate in both space and time.

5. Results and discussion

Simulations were conducted for air flowing upwards in a vertical annular pipe. The simulations concentrated on the occurrence of laminarization and property variations for high heat flux heat transfer as follows:

(1) turbulent flow with small property variations
(2) intermediate property variations
(3) large property variations with laminarization.

To obtain the above conditions, bulk Reynolds numbers of 6200, 7100, 8000, and 9700 based on the hydraulic diameter $(= 2(r_2 - r_1))$ as

$$Re = \frac{\rho_{\text{b}} u_{\text{b}} (2(r_2 - r_1))}{\mu b} \tag{39}$$

were used. The parameter r_2 and r_1 represent the outer and inner radii. And nondimensional inner wall heating

Table 1
Parameters for cases

Case	q_w	Gr	$T_b/T_{w_{in}}$	Re_{in}	r_1/r_2
1 (Aiding)	0.2×10^{-3}	23,031	0.97444	6200	0.5
2 (Aiding)	0.2×10^{-3}	35,382	0.97388	7100	0.5
3 (Aiding)	0.2×10^{-3}	98,320	0.97160	9700	0.5
3-1 (Aiding)	0.2×10^{-3}	98,320	0.97160	9700	0.5
4 (Aiding)	5×10^{-3}	1,938,787	0.40638	7100	0.3
5 (Aiding)	5×10^{-3}	5,540,896	0.37879	9700	0.3
6 (No buoy)	2×10^{-3}	875,286	0.68276	8000	0.3
7 (Aiding)	2×10^{-3}	1,100,273	0.63147	8000	0.3
8 (No buoy)	2×10^{-3}	1,094,753	0.63189	8000	0.5
9 (Aiding)	2×10^{-3}	1,234,223	0.60365	8000	0.5

rates, $q_{w_{in}}\left(=\frac{q^*_{w_{in}}}{\rho_{ref}V_{ref}T_{ref}c^*_p}\right)$, 0.75×10^{-3}, 2×10^{-3}, and 5×10^{-3} were applied. The Mach number was 0.01 and nondimensional physical time step was 0.01. Detailed conditions are tabulated in Table 1. Cases 6 and 8 both employed a dimensionless wall heat flux of 2×10^{-3} but the buoyancy term was omitted in the governing equations. Grids of $48\times48\times80$ and $96\times96\times100$ (for Case 3-1) points were used throughout this study.

The Grashof number is defined as

$$Gr=\frac{g\beta(T_{w_{in}}-T_b)(2(r_2-r_1))^3}{\nu^2} \tag{40}$$

where β represents the volumetric thermal expansion coefficient, and $T_{w_{in}}$ and T_b denote the inner wall and bulk temperatures.

The Nusselt numbers are plotted against Reynolds number as shown in Fig. 2, where the experimental correlation of turbulent heat transfer proposed by Dalle Donne and Merwald [8]

$$Nu_b=0.018\left(\frac{d_{out}}{d_{in}}\right)^{0.16}Re_b^{0.8}Pr^{0.4} \tag{41}$$

is included.

The temperature correction term for the effects of variable properties was not included due to its small variation. Torii et al. [18] found that the above correlation may only satisfy the low heat flux case and the following equation proposed by Fujii et al. [19] (also shown in Fig. 2) should be implemented for the high heat flux cases.

$$Nu_b=0.04Re_b^{2/3}Pr^{0.4} \tag{42}$$

The Nusselt number is defined as

$$Nu_b=\frac{2h(r_2-r_1)}{k_b} \tag{43}$$

where h is the heat transfer coefficient, k_b is the bulk thermal conductivity, r_1 and r_2 are the inner and outer wall radii, respectively.

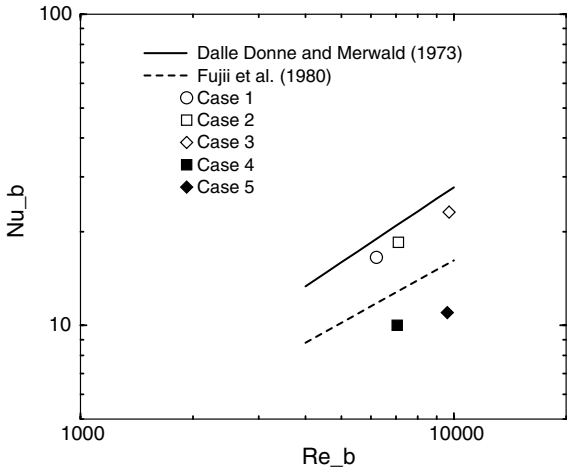

Fig. 2. Variation of Nusselt number along with correlation data.

For Cases 1, 2, and 3 (low heating cases), the deviation from Eq. (42) is seen to be minor, whilst a reasonable match is achieved with Eq. (43) for Cases 4 and 5 (high heating cases). The reduction of the Nusselt number is believed to be due to strong heating near the inner wall which leads to an increase in viscosity.

5.1. Turbulent flow with low heat transfer rates

Fig. 3 shows streamwise mean velocity profiles for the low heating cases. The radial distance is rescaled so it ranges from 0 to 2 as shown in Fig. 3. Chung et al. [7] conducted numerical simulations using DNS for the annular pipe flow with radius ratio 0.5 and the data are included for comparison. Chung et al. [7] used $Re=8900$ based on the hydraulic diameter. A fine grid case (Case 3-1) is also included to check the grid independence. As Re increases, the profiles become more flattened at the center. The current study yields good agreement with the reference data and the disagreement

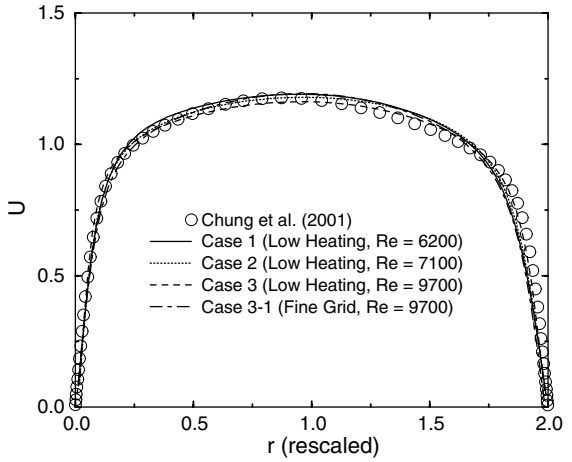

Fig. 3. Mean streamwise velocity for low heating case.

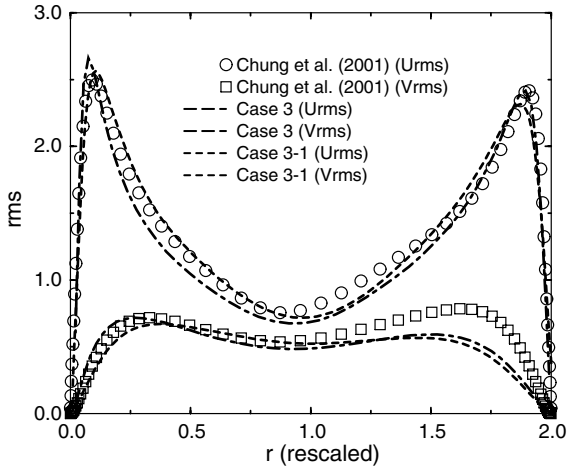

Fig. 4. Turbulent intensities for low heating case in streamwise and radial directions.

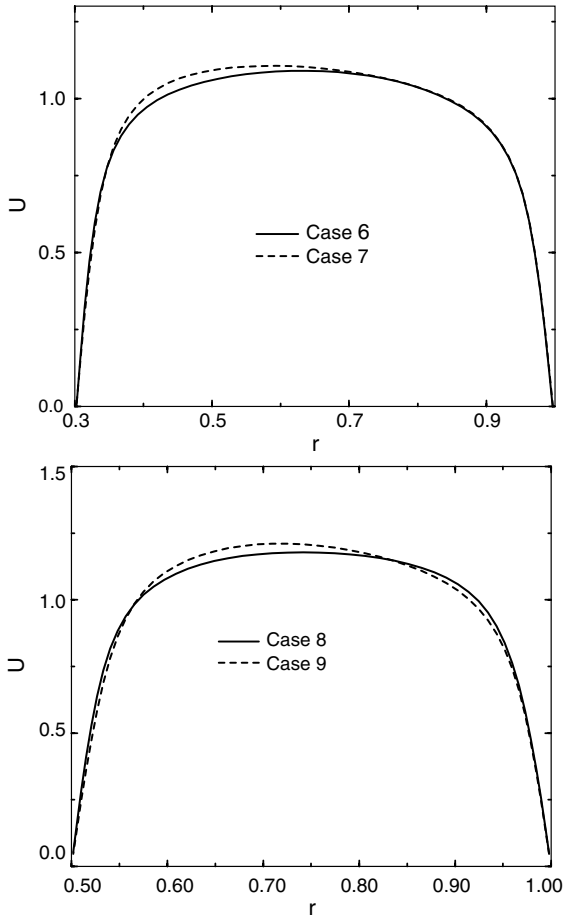

Fig. 5. Mean streamwise velocity plot for radius ratio = 0.3 and 0.5.

between the results of coarse and fine grids is fairly small.

The rms profiles (Urms and Vrms) in the streamwise and normal directions for the low heating case (Case 3) are presented in Fig. 4 along with the Chung et al. [7] profiles. Unlike the Urms plot, a significant difference is noticed in the Vrms profile near the outer wall. It seems that the differing surface areas of the inner and outer walls promote the asymmetric Vrms profile (the reduction of the Vrms values near the outer wall), but the reason for the differences between the present results and those by Chung et al. [7] is not known.

5.2. Turbulent flow with high heat transfer rates

The effect of buoyancy on the velocity distribution can be seen in Fig. 5 for the different radius ratios. The effect of buoyancy is most evident closer to the heated wall (inner wall) and the maximum velocity moves toward the heated wall. For the small radius ratio case ($r_1/r_2 = 0.3$), the maximum velocity occurs at $r = 0.6387$ and 0.5934 in the no buoyancy and aiding flow cases (Cases 6 and 7), respectively. For the radius ratio 0.5 case, the maximum occurs at $r = 0.7581$ and 0.7257 in the no buoyancy and aiding flow cases (Cases 8 and 9), respectively. The location of the maximum velocity will be discussed when the shear stress and turbulent heat flux ($\overline{u'T'}$) profiles are presented later in this paper.

The distribution of the Reynolds shear stress is shown in Fig. 6 for Cases 6 and 7, where a large buoyancy influence is observed. Hall and Jackson [20] found that a reduction of the shear stress in the aiding flow results in the decrease in the production of the turbulent kinetic energy and eventual laminarization.

The locations for zero shear stress and the maximum velocity for different radius and level of buoyancy cases are different as shown in Table 2. The point where the

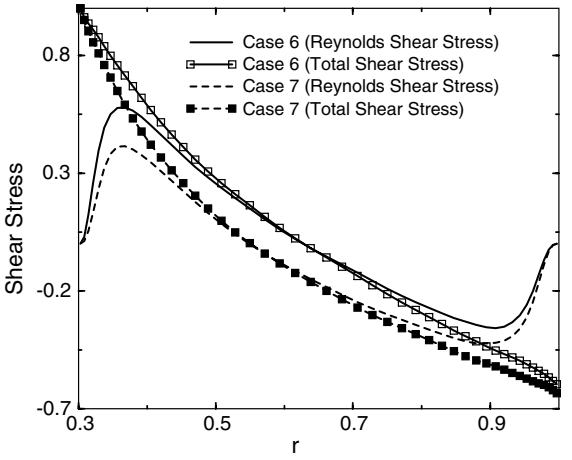

Fig. 6. Shear stress plot for radius ratio = 0.3.

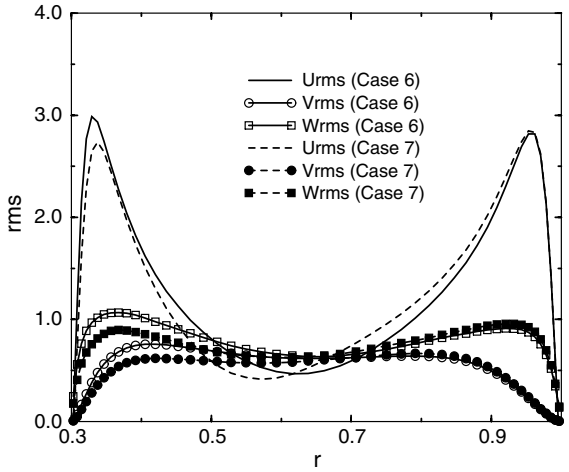

Fig. 7. Turbulent intensity plot for radius ratio = 0.3.

Table 2
Locations of zero shear stress and maximum mean velocity

Case	r_{shear}	$r_{velocity}$
6	0.64154871	0.6386129
7	0.5736087	0.5934346
8	0.76720128	0.7581337
9	0.71100523	0.7256522

shear stress vanishes has been generally assumed to coincide with the location of the maximum velocity [20], but those two points are not same in the case of turbulent flow in annuli [21]. As shown in Table 2, the position of zero crossing shear stress, r_{shear}, is closer to the inner wall (heated wall) than the location of the maximum velocity, $r_{velocity}$, in the aiding flow, but the locations of maximum mean velocity for no buoyancy cases (Cases 6 and 8) are closer to the inner wall. The buoyancy force near the heated wall reduces the distance of the zero crossing shear stress more effectively than that of maximum velocity.

Fig. 7 compares the radial distributions of turbulent intensities. Closer to the heated wall, the profiles tend to decrease showing the aiding flow effects for both radius ratio cases. However, close to the outer wall (adiabatic wall), the profiles tend to merge. The turbulent heat fluxes of $\overline{u'T'}$ and $\overline{v'T'}$ are plotted in Figs. 8 and 9. In this study, v' represents the velocity fluctuations in the radial direction. For the small radius ratio cases (Cases 6 and 7), the buoyancy effects do not cause the profile to deviate much from the no buoyancy case, but the heating with buoyancy for the large radius ratio cases (Cases 8 and 9) has enhanced the magnitudes of both plots sharply. Another noticeable characteristic is the zero crossing location of $\overline{u'T'}$ as mentioned before. The zero $\overline{u'T'}$ occurs at $r = 0.6575$ and $r = 0.5801$ without and

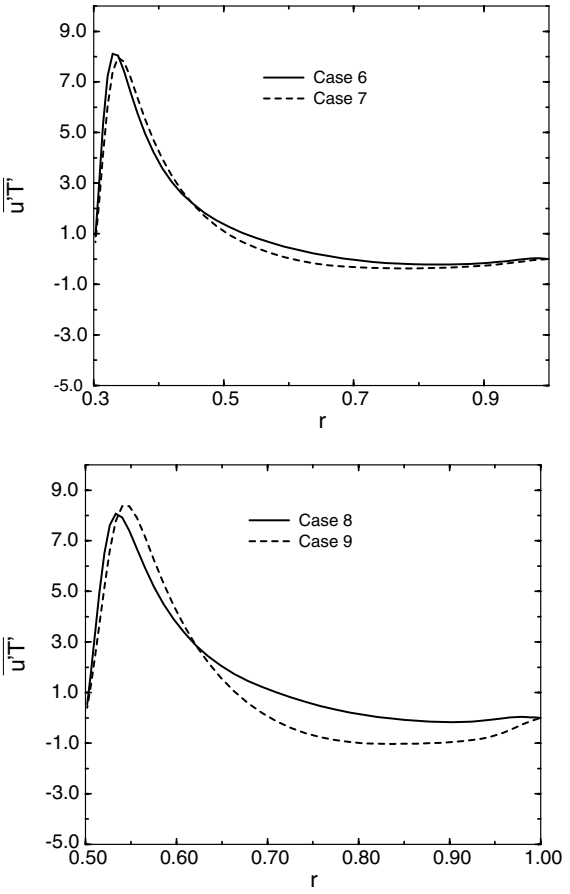

Fig. 8. Streamwise turbulent heat flux plot for radius ratio = 0.3 and 0.5.

with buoyancy for the small radius ratio cases (Cases 6 and 7), respectively. Similarly, it occurs at $r = 0.7654$

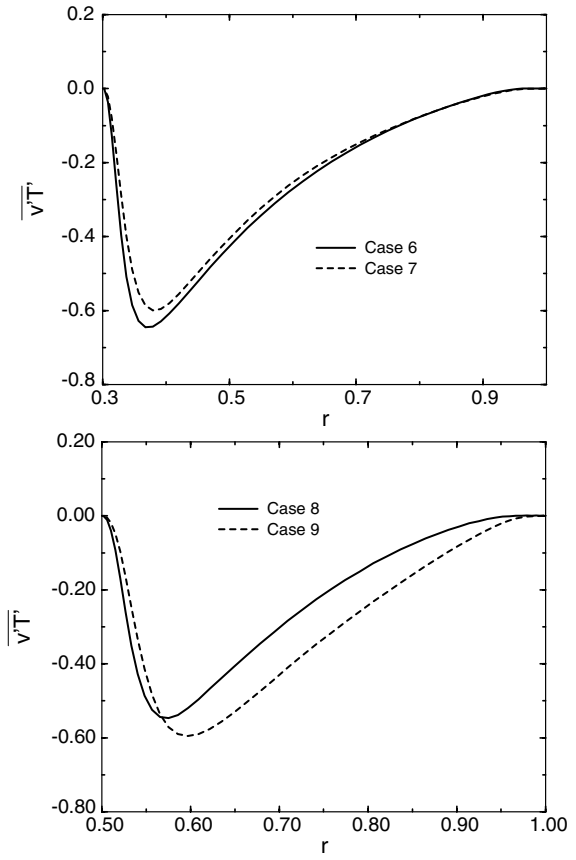

Fig. 9. Normal turbulent heat flux plot for radius ratio = 0.3 and 0.5.

and $r = 0.7034$ for the large radius ratio cases (Cases 8 and 9). Again, the buoyancy effect is shown to move the location of zero turbulent heat flux closer to the heated wall side (inner wall).

For strongly heated flow, the occurrence of laminarization may be possible. The criteria of flow laminarization can be estimated by use of an equivalent bulk flow acceleration [18,22]. The bulk flow acceleration parameter, K, is defined as

$$K = \frac{4q_{w_{in}}}{Re_{in}}\left(1 + 4q_{w_{in}}\frac{x}{d}\right)^{-0.43}\left(\frac{d_{in}}{d_{out} + d_{in}}\right) \tag{44}$$

and Coon et al. [23] proposed the condition of transition as $K > 1.5 \times 10^{-6}$. Fig. 10 shows the correlation for transition. It suggests that the transitional state may exist for Cases 4, 5, and 7 due to high heating but the flow may remain turbulent for Cases 1, 2 and 3. According to Torii et al. [18], the laminarization from the heated wall is suppressed by the turbulent production near the insulated wall and it is quite unusual to have laminarized flow in an annular pipe heated only on one side.

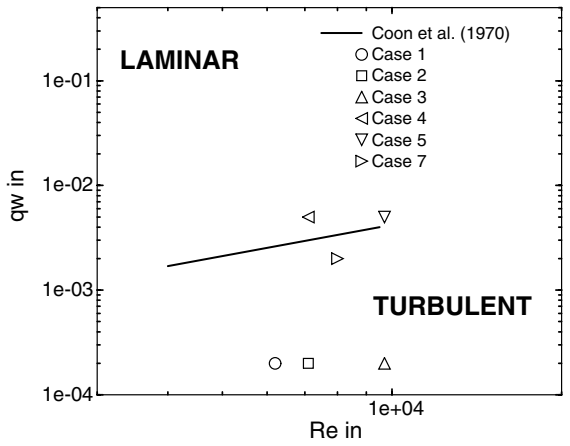

Fig. 10. Comparison with proposed criteria for laminarization.

6. Conclusions

Simulations were performed for air flowing upwards in a vertical annular pipe. The simulations were concerned with the occurrence of laminarization and the effects of property variations for high heat flux heat transfer.

For the low heating cases, the deviation from the *Nu* correlation proposed by Dalle Donne and Merwald [8] was observed to be minor, but severe impairment of heat transfer was observed as buoyancy influences built up for high heating cases. This reduction is believed to be due to strong heating near the inner wall which leads to an increase in viscosity and the consequential enhancement in the damping of turbulence.

Variations in the streamwise velocity distribution due to the influence of buoyancy were evident near the heated wall (inner wall) and the velocity near the center was reduced as the maximum velocity moved toward the heated wall. Similarly, a large buoyancy influence was observed in the distribution of the Reynolds shear stress. The position of zero crossing shear stress was closer to the inner wall (heated wall) than the location of the maximum velocity in the aiding flow, but the location of maximum mean velocity for the no buoyancy cases was closer to the inner wall.

The turbulent intensities tended to decrease near the heated wall indicating buoyancy effects for both radius ratio cases. However, close to the outer wall (adiabatic wall), the profiles of intensities tended to merge.

The effect of buoyancy in $\overline{u'T'}$ and $\overline{v'T'}$ was more noticeable for the larger radius ratio cases than for the smaller radius ratio cases. Another noticeable characteristic was the zero crossing location of $\overline{u'T'}$. The zero $\overline{u'T'}$ occurred at $r = 0.6575$ and $r = 0.5801$ without buoyancy and with buoyancy for the small radius ratio cases (Cases 6 and 7), respectively. Similarly, zero

crossing occurred at $r = 0.7654$ and $r = 0.7034$ for the large radius ratio cases (Cases 8 and 9), respectively. Again, the buoyancy effect was shown to move the zero crossing location closer to the heated wall side (inner wall).

Complete laminarization was not observed in this study even for the high heating cases. Laminarization was believed to be suppressed by the turbulent production near the insulated wall.

Acknowledgements

The authors are grateful to the National Science Foundation (NSF) and the Department of Energy under the NERI program for support through grants CTS-9806989 and DE-FG03-995F21924. The Iowa State High Performance Computing Center and University of the Minnesota Supercomputing Institute provided computational resources needed for this research.

References

[1] D.P. Mikielewicz, Comparative studies of turbulence models under conditions of mixed convection with variable properties in heated vertical tubes, PhD thesis, Univ. Manchester, UK, 1994.
[2] M. Nakajima, K. Fukui, H. Ueda, T. Mizushina, Buoyancy effects on turbulent transport in combined free and forced convection between vertical parallel plates, Int. J. Heat Mass Transfer 23 (1979) 1325–1336.
[3] A.F. Polyakov, Transient effects due to thermogravity in turbulence and heat transfer, Heat Transfer—Sov. Res. 11 (1973) 90–98.
[4] J.A. Zarate, M. Capizzani, R.P. Roy, Velocity and temperature wall laws in a vertical concentric annular channel, Int. J. Heat Mass Transfer 41 (1998) 287–292.
[5] J. Kim, P. Moin, Transport of passive scalars in a turbulent channel flow, in: Turbulent Shear Flows, vol. 6, Springer-Verlag, 1989.
[6] O. Iida, N. Kasagi, Direct numerical simulation of unsteady stratified turbulent channel flow, J. Heat Transfer 119 (1997) 53–61.
[7] S.Y. Chung, G.H. Rhee, H.J. Sung, Direct numerical simulation of turbulent concentric annular pipe flow turbulence and shear flow phenomena, Stockholm, 27–29 June 2001, pp. 377–382.
[8] M. Dalle Donne, E. Merwald, Heat transfer friction coefficients for turbulent flow of air in smooth annuli at high temperature, Int. J. Heat Mass Transfer 16 (1973) 787.
[9] S. Torii, A. Shimizu, S. Hasegawa, N. Kusama, Convective heat transfer in annular passages with high heat flux, Heat Transfer Japanese Res. 16 (1988) 46.
[10] G. Erlebacher, M.Y. Hussaini, C.G. Speziale, T.A. Zang, Toward the large-eddy simulation of compressible turbulent flows, ICASE Report 90-76, NASA Langley Research Center, 1990.
[11] A.W. Vreman, B.J. Geurts, J.G.M. Kuerten, P.J. Zandbergen, A finite volume approach to large eddy simulation of compressible, homogeneous, isotropic, decaying turbulence, Int. J. Numer. Meth. Fluids 15 (1992) 799–816.
[12] M. Germano, U. Piomelli, P. Moin, W. Cabot, A dynamic subgrid-scale eddy viscosity model, Phys. Fluids A 3 (1991) 1760–1765.
[13] P. Moin, K. Squires, W. Cabot, W.S. Lee, A dynamic subgrid-scale model for compressible turbulent and scalar transport, Phys. Fluids 3 (1991) 2746–2757.
[14] W.P. Wang, Coupled compressible and incompressible finite volume formulations for the large eddy simulation of turbulent flow with and without heat transfer, PhD thesis, Iowa State University, Ames, IA, 1995.
[15] D.K. Lilly, A proposed modification of the germano subgrid-scale closure method, Phys. Fluids A 4 (1992) 633–635.
[16] L.D. Dailey, Large eddy simulation of turbulent flows with variable property heat transfer using a compressible finite volume formulation, PhD thesis, Iowa State University, Ames, IA, 1997.
[17] X. Xu, J.S. Lee, R.H. Pletcher, Cartesian based finite volume formulation for LES of mixed convection in a vertical turbulent pipe flow, ASME IMECE, New Orleans, LA, 17–22 November 2002.
[18] S. Torii, A. Shimizu, S. Hasegawa, N. Kusama, Laminarization of strongly heated annular gas flows, Int. J. JSME (1991) 157–168.
[19] S. Fujii, M. Hisida, H. Kawamura, N. Akino, 17th National Heat Transfer Symp., Japan, 1980.
[20] W.B. Hall, J.D. Jackson, Laminarization of a turbulent pipe flow by buoyancy forces, ASME paper no. 69-HT-55, 1969.
[21] S. Satake, H. Kawamura, Large eddy simulation of turbulent flow in concentric annuli with a thin inner rod, Turbulent Shear Flow 9, Berlin, 1995, pp. 259–281.
[22] D. McEligot, C.W. Coon, H.C. Perkins, Relaminarization in tubes, Int. J. Heat Mass Transfer 13 (1970) 431–433.
[23] C.W. Coon, H.C. Perkins, Transition from the turbulent to laminar regime for internal convective flow with large property variations, Trans. ASME Ser. C 92 (1970) 506–512.